





REGULAR PAPER

A deep learning-based approach to time-coordination entry guidance for multiple hypersonic vehicles

Z. Li, J. Guo*, S. Tang  and S. Ji 

Key Laboratory of Dynamics and Control of Flight Vehicle, Ministry of Education, School of Aerospace Engineering, Beijing Institute of Technology, Beijing 100,081, China

*Correspondence author. Email: guojie1981@bit.edu.cn

Received: 22 December 2021; **Revised:** 24 August 2022; **Accepted:** 3 September 2022

Keywords: Hypersonic glide vehicles; Cooperative entry guidance; Neural network; Deep learning; Extended Kalman filter

Abstract

A multiple-vehicles time-coordination guidance technique based on deep learning is suggested to address the cooperative guiding problem of hypersonic gliding vehicle entry phase. A dual-parameter bank angle profile is used in longitudinal guiding to meet the requirements of time coordination. A vehicle trajectory database is constructed along with a deep neural network (DNN) structure devised to fulfill the error criteria, and a trained network is used to replace the conventional prediction approach. Moreover, an extended Kalman filter is constructed to detect changes in aerodynamic parameters in real time, and the aerodynamic parameters are fed into a DNN. The lateral guiding employs a logic for reversing the sign of bank angle, which is based on the segmented heading angle error corridor. The final simulation results demonstrate that the built DNN is capable of addressing the cooperative guiding requirements. The algorithm is highly accurate in terms of guiding, has a fast response time, and does not need inter-munition communication, and it is capable of solving guidance orders that satisfy flight requirements even when aerodynamic parameter disruptions occur.

Nomenclature

CAV	Common Aero Vehicle
DNN	Deep Neural Network
DQN	Deep Q Network
DOF	Degree of Freedom
EKF	Extended Kalman Filter
HTV	Hypersonic Technology Vehicle
HGV	Hypersonic Glide Vehicle
QEGC	Quasi-equilibrium Glide Condition

1.0 Introduction

Hypersonic glide vehicles (HGV) flying in near space rely mainly on aerodynamic force for control and have a Mach number greater than 5 [1]. The entry phase of the hypersonic glide vehicle has the characteristics of high speed, a wide range of speed change, long-range and high manoeuvrable. Typical HGVs are the common aero vehicle (CAV) [2] and hypersonic technology vehicle (HTV) [3]. In response to the threats posed by hypersonic vehicles, various countries have successively developed anti-missile interception systems such as Aegis and S-400, which greatly weakens the combat effectiveness and penetration capabilities of hypersonic vehicles [4]. To improve the penetration capability of hypersonic vehicles and achieve saturation strikes on targets, it is necessary to develop multi-hypersonic vehicles coordinated strike technology.

The flight process of the HGV is divided into five phases: boot-up, adjustment, initial entry, entry glide and attack down [5]. Among them, the entry gliding phase has the longest flight distance, the largest airspace span, and the most dramatic changes in aerodynamic characteristics. The complexity of the state change during the vehicle's entry phase will have a huge impact on the terminal guidance phase. Therefore, it is reasonable to conduct time-coordinated guidance of the vehicle in the entry phase, so that multiple vehicles can provide good handover conditions for the coordination of the next terminal guidance phase and finally reach the designated target point at the same time.

The existing entry guidance methods mainly include nominal trajectory guidance and predictive correction guidance. Shen and Lu [6] obtained the constrained boundary of the bank angle according to the height-speed entry corridor and obtained the nominal trajectory of the gliding phase by designing the bank angle curve that met these requirements. Zhang et al. [7] studied the trajectory planning method based on the three-dimensional drag acceleration profile. For predictive correction guidance, based on a consideration of the path constraints, Joshi et al. [8] used the angle-of-attack and the bank angle as the control variables of the prediction-correction guidance method. However, the above-mentioned guidance methods apply to a single vehicle and cannot be directly used to the coordinated guidance of multi-hypersonic vehicles.

Current multi-vehicle coordinated guidance methods are mostly applied to terminal guidance [9] or low-speed unmanned aerial vehicles [10, 11, 12]; in terms of multi-missile cooperative guidance, the existing cooperative guidance methods can be divided into a two-layer cooperative guidance architecture and a "leader-follower" cooperative guidance architecture. Zhao et al. [13] proposed a two-layer guidance architecture for the first time, in which the constrained guidance law satisfying the missile flight characteristics was the bottom-level guidance control, and the centralised or decentralised coordination strategy including coordination variables was used as the upper-level coordination control. Zhang et al. [14] proposed the leader-follower cooperative guidance architecture, which selected the reference motion state of the missile according to the coordination requirements, and took the lead missile as the desired reference motion state. By tracking the reference motion state of the leading missile or adjacent ballistics, the reference motion state of the secondary missile gradually adjusted to the expected value, thereby realising multi-missile cooperative guidance. Subsequent research was mostly based on the optimisation of the above two architectures. For stationary targets in the plane, Kumar et al. [15] designed a time-constrained guidance law based on sliding mode control as the bottom layer guidance control, and the upper layer coordinated control was based on the minimum sum of the sliding mode surface deviations of all missiles to obtain cooperative guidance method with expected attack time as average of remaining time. Compared with traditional missiles, HGVs have unique difficulties such as fast flight speed and single control amount. For the hypersonic vehicle entry phase, coordinated guidance can be separated into two types: lateral guidance and longitudinal guidance. For lateral guidance, Liang et al. [16] used the shooting method to optimise the longitudinal bank angle profile to meet the terminal distance and height constraints, and laterally through the iterative heading angle corridor width to meet the coordination time constraints. Yu et al. [17] proposed an analytical multi-projectile coordinated entry guidance method. This method divided the entry trajectory into two sections. The first section adopted a plan for the angle-of-attack, and the iterative bank angle satisfied the distance constraint. The second section had a bank angle of zero and the iterative angle-of-attack met the time constraint. But this method was not suitable for HGVs with drastic changes in lift-to-drag ratio. Fang et al. [18] proposed a time-controllable entry guidance law, which used neural networks to predict the remaining flight time and increased the lateral manoeuvrability by adjusting the heading angle and corridor width to change the flight time. Zhang et al. [19] proposed a deep reinforcement-based entry cooperative guidance method. The longitudinal lift-to-drag ratio was calculated to obtain the modulus of bank angle based on the high-precision longitudinal analytical solution. In lateral guidance, the DQN algorithm was used to adjust the sign of the pitch angle to control the flight time. The above-mentioned time-coordination guidance algorithms all change the flight time by increasing the lateral manoeuvrability of the vehicle and increasing the lateral manoeuvrability might cause the vehicle to miss the target or result in problems in avoiding obstacles. For longitudinal guidance, Wang et al. [20] proposed a predictive-corrected cooperative guidance law based on the altitude-velocity profile, which adjusted the remaining flight time and distance by

adjusting the two trajectory parameters of the profile and further analysed the ability of co-time regulation. Li et al. [21] proposed a time-coordination guidance algorithm based on the bank angle profile, the time and range constraints were met by adjusting the parameter values of the bank angle profile, and at the same time by adjusting the lateral error damping coefficient in the lateral direction, and the time adjustment capability was further increased. But the change range of adjustment parameters of the algorithm were too large to put it into real practice. The above two time-coordinated guidance algorithms based on longitudinal guidance have real-time problems due to the large number of integral prediction and it cannot meet the requirements of rapid guidance of hypersonic vehicles at high Mach numbers.

Based on the above analysis, this paper proposes a time-coordination entry guidance algorithm based on deep learning. First, a dual-parameter bank angle profile is developed to suit the requirements of time coordination and to set the groundwork for the vehicle trajectory database’s compilation. Second, a vehicle trajectory database is built, and a framework is developed for a deep neural network (DNN) that satisfies the error criteria to identify the functional relationship between the flight states and the parameters of the profile in longitudinal guidance, which improves the real-time performance of the algorithm. Moreover, the input parameters of the deep neural network contain perturbations in the lift and drag coefficients that significantly improve the algorithm’s resilience. Finally, the extended Kalman filter (EKF) is used to identify the disturbance coefficients online, and to meet the needs of the real flight process, the disturbance coefficients are used as input parameters for the DNN training in the network design.

2.0 Preliminary

2.1 System dynamics

In the entry phase of the vehicle, in order to grasp the main contradiction, the following assumptions are made: the rotation of the Earth is not considered; considering that the longitudinal range of the entry phase is relatively large, the Earth is regarded as a sphere. The 3DOF point-mass dynamics for hypersonic entry vehicle over a non-rotating Earth are described by [22]:

$$\begin{cases} \dot{r}_i = V_i \sin \theta_i \\ \dot{\lambda}_i = \frac{V_i \cos \theta_i \sin \psi_i}{r_i \cos \phi_i} \\ \dot{\phi}_i = \frac{V_i \cos \theta_i \cos \psi_i}{r_i} \\ \dot{V}_i = -D_i - g \sin \theta_i \\ \dot{\theta}_i = \frac{1}{V_i} \left[L_i \cos \sigma_i + \left(\frac{V_i^2}{r_i} - g \right) \cos \theta_i \right] \\ \dot{\psi}_i = \frac{1}{V_i} \left(\frac{L_i \sin \sigma_i}{\cos \theta_i} + \frac{V_i^2}{r_i} \cos \theta_i \sin \psi_i \tan \phi_i \right) \\ \dot{t}_i = 1 \end{cases} \tag{1}$$

where i represents the i th vehicle; r is the nondimensional radial distance from the Earth’s centre to the vehicle, the nondimensional parameter is the radius of the earth R_0 ; λ and ϕ are the longitude and latitude; V is the Earth-relative nondimensional velocity; $\sqrt{g_0 R_0}$ is the nondimensional parameter; g_0 is the gravitational acceleration at sea level; θ is the flight-path angle of the Earth-relative velocity vector; ψ is the heading angle of the same velocity vector; t is the time of vehicle flight; σ is the bank angle of the vehicle about the relative velocity vector; L and D are the nondimensional lift and drag acceleration, they are shown in the Equation (2):

$$\begin{cases} L = 0.5S\rho V^2 C_L/m \\ D = 0.5S\rho V^2 C_D/m \end{cases} \tag{2}$$

where m is the vehicle mass; S is the vehicle reference area; $\rho = \rho_0 e^{-h/7110}$ is the atmospheric density, ρ_0 is the atmospheric density at sea level, h is the distance from the ground to the vehicle; C_L and C_D are the lift coefficient and the drag coefficient, and they are a nonlinear function of the Mach number and angle-of-attack. Aerodynamic data can be obtained from the references [23].

An energy-like variable e as the independent variable of the prediction and the input of the DNN:

$$e = 1/r - V^2/2 \tag{3}$$

$$\dot{e} = DV \tag{4}$$

It is clear that e is the negative of the specific mechanical energy used in orbital mechanics, and it is a monotonically increasing variable [24].

2.2 Entry trajectory constraints

The typical path constraints of an entry vehicle include the heating rate limit $\dot{Q}_{\max,i}$, the aerodynamic overload limit $n_{\max,i}$, the dynamic pressure limit $q_{\max,i}$, and they can be expressed as [25]:

$$\dot{Q}_i = k_{Q,i} \rho_i^{0.5} V_i^3 \leq \dot{Q}_{\max,i} \tag{5}$$

$$n_i = \sqrt{L_i^2 + D_i^2} \leq n_{\max,i} \tag{6}$$

$$q_i = \frac{1}{2} g_{0,i} \rho_i V_i^2 \leq q_{\max,i} \tag{7}$$

where \dot{Q}_i is the heating rate and $k_{Q,i}$ is a constant, n_i is the aerodynamic overload and q_i is the dynamic pressure. The above constraints are hard constraints for an entry vehicle, and the vehicle also needs to meet the quasi-equilibrium guide condition (QEGC) soft constraint

$$L_i \cos \sigma_{QEGC,i} - \left(V_i^2 - \frac{1}{r_i} \right) \frac{\cos \theta_i}{r_i} \geq 0 \tag{8}$$

where $\sigma_{QEGC,i}$ is the bank angle of the vehicle in QEGC, generally the value is zero.

The typical final constraints are that the trajectory reaches the final longitude $\lambda_{f,i}$ and latitude $\varphi_{f,i}$ at a specified final altitude $r_{f,i}$ and velocity $V_{f,i}$, it can be shown that

$$\begin{cases} r(t_{f,i}) = r_{f,i} \\ V(t_{f,i}) = V_{f,i} \\ \lambda(t_{f,i}) = \lambda_{f,i} \\ \varphi(t_{f,i}) = \varphi_{f,i} \end{cases} \tag{9}$$

where $t_{f,i}$ is the time of the vehicle entry phase, $r_{f,i}$ is the terminal radial distance from the Earth's centre to the vehicle, $V_{f,i}$ is the terminal Earth-relative velocity, $\lambda_{f,i}$ is the terminal longitude, $\varphi_{f,i}$ is the terminal latitude. Regarding the question of the entry vehicles guidance, the final constraints of the longitude and the latitude usually transform a distance s_f from the target location.

Considering the time-coordination problem of multi-hypersonic vehicles, it is also necessary to meet the terminal time constraints, which can be expressed as:

$$t_{f,1} = t_{f,2} = \dots = t_{f,i} = t_{co} \tag{10}$$

where $t_{f,i}$ is the total time of entry flight, t_{co} is the prescribed coordination time [21].

Therefore, the objective of time-coordination entry guidance is based on the 3DOF point-mass dynamics Equation (1) to obtain the adjustment parameters of the bank angle profile that meet the constraints Equations (5)–(10).

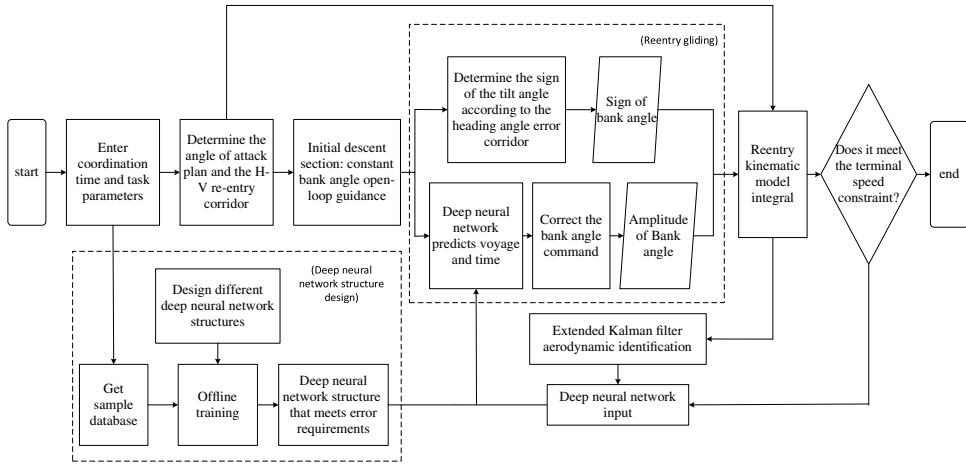


Figure 1. Flowchart of the proposed time-coordination entry guidance algorithm.

3.0 Time-coordination guidance algorithm based on DNN

A traditional predictor-corrector guidance algorithm consists of two parts: longitudinal guidance and lateral guidance. Longitudinal guidance determines the amplitude of the bank angle, and lateral guidance uses the heading angle error corridor to determine the bank angle sign.

The longitudinal guidance is composed of two parts: prediction and correction. There is a large amount of integration in the longitudinal guidance of vehicles, and there are real-time problems that cannot be ignored for hypersonic vehicles. The traditional predictor-corrector guidance algorithm can only predict the remaining distance, and cannot meet the needs of coordinated flight of hypersonic vehicles. During the entry process, there will be aerodynamic parameter disturbances, and the hypersonic vehicle mainly relies on aerodynamic force to achieve the entry mission. The aerodynamic parameter disturbances will have a great impact on the accuracy of trajectory prediction and the successful completion of the entry mission.

To solve the cooperative flight problem of vehicles, this paper constructs an improved bank angle profile, which can accurately predict of the remaining distance and remaining time at the same time, so that multiple vehicles can simultaneously reach the designated target point. For real-time problems, this paper designs the DNN to identify the functional relationship between the flight states and the adjustment parameters of the bank angle profile in the predictor-corrector, thereby effectively shortening the guidance instruction solution time and improving the algorithm real-time react ability. For the robustness problem, in the design of the DNN, the influence of atmospheric disturbance is considered to improve the guidance accuracy of the algorithm, and all the aerodynamic parameters are identified online using the EKF. The algorithm flowchart is shown in Fig. 1.

3.1 Angle-of-attack profile design

The control amount of the hypersonic vehicle entry flight phase is the angle-of-attack α and the bank angle σ . Considering the thermal protection requirements of the initial phase of entry and the remaining flight distance requirements, this study adopts the angle-of-attack profile is shown as [26]:

$$\alpha = \begin{cases} \alpha_m & V > V_1 \\ \frac{\alpha_{L/D_{max}} - \alpha_m}{V_b - V_a} (V - V_a) + \alpha_m & V_2 \leq V \leq V_1 \\ \alpha_{L/D_{max}} & V < V_2 \end{cases} \quad (11)$$

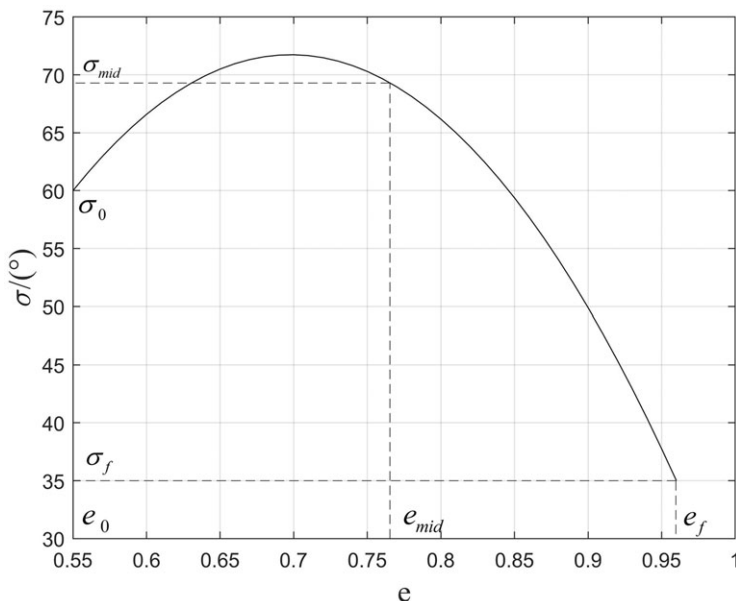


Figure 2. Bank angle profile of two adjustment parameters.

where α_m is the maximum angle-of-attack, $\alpha_{L/D_{max}}$ is the maximum lift-to-drag ratio angle-of-attack, V_a , V_b , V_1 and V_2 are the set speed value; $V_a = 6,500m/s$, $V_b = 5,000m/s$, $V_1 = 7,000m/s$ and $V_2 = 5,400m/s$.

3.2 Dual-parameter bank angle profile design

For the initial descent phase of the entry vehicle, the altitude of the vehicle is high, and the aerodynamic effect is small, and it is difficult to effectively control the trajectory of the vehicle. Normally, open-loop guidance with a constant tilt angle is used. After meeting the QEGC, the vehicle moves to the gliding phase. The bank profile of the gliding phase of the HGV is usually designed as a single parameter to meet the needs of adjusting the flight distance. In this section, the vehicle bank angle profile is designed as a parabolic dual-parameter profile, and the time and distance are adjusted at the same time to meet the needs of time-coordinated guidance. For the longitudinal guidance of the gliding phase, the dual-parameter bank angle profile is shown in Fig. 2. In Fig. 2, when the three points on the curve are known, the curve equation can be determined. Therefore, the horizontal and vertical coordinates corresponding to the three points can be used as characteristic values for determining the shape of the curve. When four of the values are determined, the remaining two can be used as adjustment parameters to adjust the remaining flight time and distance. The curve function is defined as shown in Equation (12)

$$|\sigma(e)| = k_1e^2 + k_2e + k_3 \tag{12}$$

where k_1 , k_2 and k_3 are the bank angle profile coefficient, they can be determined by Equation (13)

$$\begin{cases} \sigma_0 = k_1e_0^2 + k_2e_0 + k_3 \\ \sigma_{mid} = k_1e_{mid}^2 + k_2e_{mid} + k_3 \\ \sigma_f = k_1e_f^2 + k_2e_f + k_3 \end{cases} \tag{13}$$

where σ_0 , σ_{mid} and σ_f are the initial bank angle of the gliding phase, the bank angle at the midpoint, and the terminal bank angle of the gliding phase. e_0 is the initial energy and it is determined by the

state of the vehicle after the end of the initial descent, e_f is terminal energy and it determined by terminal geocentric $r_{f,i}$ distance and terminal velocity $V_{f,i}$, e_{mid} is the midpoint energy, as shown in the Equation (14):

$$e_{mid} = (e_0 + e_f)/2 \tag{14}$$

Equation (13) is a system of linear equations with three variables $k_i(i = 1, 2, 3)$ and three equations. Therefore, according to the Cramer’s rule, the value of k_1, k_2 and k_3 can be obtained:

$$k_1 = \frac{\begin{vmatrix} \sigma_0 & e_0 & 1 \\ \sigma_{mid} & e_{mid} & 1 \\ \sigma_f & e_f & 1 \end{vmatrix}}{\begin{vmatrix} e_0^2 & e_0 & 1 \\ e_{mid}^2 & e_{mid} & 1 \\ e_f^2 & e_f & 1 \end{vmatrix}}, k_2 = \frac{\begin{vmatrix} e_0^2 & \sigma_0 & 1 \\ e_{mid}^2 & \sigma_{mid} & 1 \\ e_f^2 & \sigma_f & 1 \end{vmatrix}}{\begin{vmatrix} e_0^2 & e_0 & 1 \\ e_{mid}^2 & e_{mid} & 1 \\ e_f^2 & e_f & 1 \end{vmatrix}}, k_3 = \frac{\begin{vmatrix} e_0^2 & e_0 & \sigma_0 \\ e_{mid}^2 & e_{mid} & \sigma_{mid} \\ e_f^2 & e_f & \sigma_f \end{vmatrix}}{\begin{vmatrix} e_0^2 & e_0 & 1 \\ e_{mid}^2 & e_{mid} & 1 \\ e_f^2 & e_f & 1 \end{vmatrix}} \tag{15}$$

where σ_0 is designed as a definite value, e_0, e_{mid} and e_f are definite values. The remaining flight distance and time of the vehicle are adjusted by adjusting the values of σ_{mid} and σ_f .

3.3 Determining the amplitude of bank angle based on DNN

Artificial intelligence technology has gradually matured in recent years, owing to advancements in computer software and hardware. The purpose of this paper is to demonstrate how deep learning in artificial intelligence technology can be used to enhance the real-time performance of collaborative guidance algorithms. Proposed by Hinton et al. [27] in 1986, deep learning replaced the original single fixed feature layer with multiple hidden layers. The activation function used the Sigmoid function, and the error backpropagation algorithm was used to train the model. The network obtained by deep learning had a multi-layer structure, and each layer had multiple neurons. The network structure that met the requirements could be obtained by adjusting the weight relationship among the neurons. At present, deep learning is mostly used in low-speed unmanned aerial vehicles [28, 29] and less in hypersonic aircraft. In this paper, the trained DNN can be used to fit the non-linear mapping relationship between the input and output in the prediction.

After combining the bank angle profile in Equation (12) of the traditional prediction, the remaining distance and time can be obtained by establishing a longitudinal motion equation shown as Equation (16) with non-dimension energy as the independent variable

$$\begin{cases} \frac{ds}{de} = \frac{\cos \theta}{rD} \\ \frac{dr}{de} = \frac{\sin \theta}{D} \\ \frac{d\theta}{de} = \left[L \cos \sigma + \left(V^2 - \frac{1}{r} \right) \frac{\cos \theta}{r} \right] \frac{1}{DV^2} \\ \frac{dt}{de} = \frac{1}{DV} \end{cases} \tag{16}$$

where $V = \sqrt{2(1/r - e)}$.

From the analysis of Equation (16), it can be seen that the input of the DNN is: the non-dimension energy e , the nondimensional radial distance r , the flight-path angle θ , the bank angle σ , the nondimensional aerodynamic lift acceleration L and drag acceleration D . The bank angle is determined by the bank angle adjustment parameters σ_{mid} and σ_f . Considering that the vehicle is in a real flight environment, the aerodynamic parameters are disturbed compared to the those in normal conditions, the lift acceleration and the drag acceleration are affected by the disturbance coefficients k_{cl} and k_{cd} . Therefore,

Table 1. Initial state quantity change table

Amount of change	Change interval	Step size
$\theta/(\text{°})$	$[-0.004, 0.004]$	0.002
k_{cl}	$[0.9, 1.1]$	0.1
k_{cd}	$[0.9, 1.1]$	0.1
$\sigma_{mid}/(\text{°})$	$[50, 80]$	1
$\sigma_f/(\text{°})$	$[10, 40]$	1

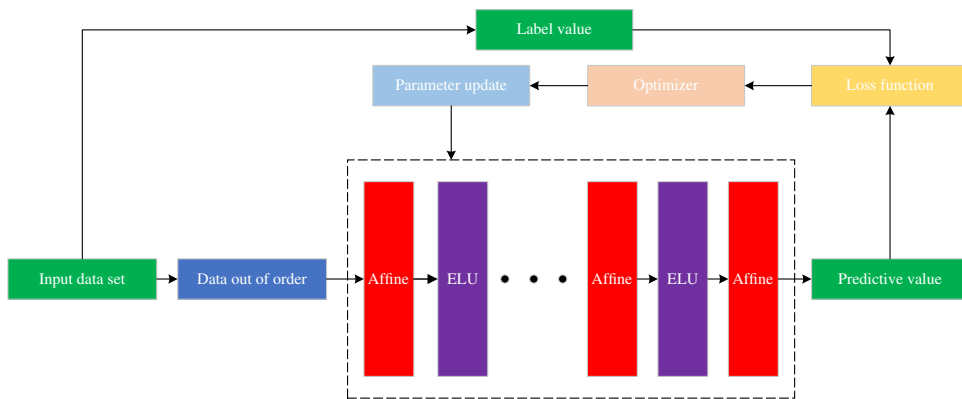


Figure 3. The structure of the DNN.

the input of the DNN is: $x_{NN} = [e \ r \ \theta \ \sigma_{mid} \ \sigma_f \ k_{cl} \ k_{cd}]$; output is: $y_{NN} = [s \ t]$. Considering that DNN is sensitive to input data, the upper and lower bounds of the input data should not exceed the upper and lower bounds of the training data, as shown in Table 1. The range of energy is $[0.5552, 0.9637]$, and the range of nondimensional radial distance is $[1.0089, 1.0044]$.

The first prerequisite for training a DNN is to obtain a reliable data set. This paper uses Equation (16) to obtain the DNN data set. Choosing $e = 0.5552$ and $r = 1.0089$ as the initial state, the bank angle adjustment parameters σ_{mid} and σ_f , aerodynamic parameter disturbance coefficient k_{cl} and k_{cd} , and the flight-path angle θ as the initial state change, are shown in Table 1.

The fourth-order Runge-Kutta integration according to the Equation (16) is performed to obtain the reentry trajectories in different initial states, taking 60 points on each trajectory and generating 4,095,000 pairs of data for creating a database of HGV trajectory points. In the database, 90% pairs of data are randomly selected for the training set, and the remaining 10% pairs of data are used for the test set.

The problem outlined in this paper is a regression problem in deep learning. After obtaining the data set required for training, the designed DNN structure is shown in Fig. 3. In a DNN, the number of hidden layers and units in each layer need to be determined first. The deeper the number of layers of the DNN, the higher the number of neurons in each layer, the more complicated the calculation process that can be replaced, and the higher the approximation accuracy. However, as the number of layers and neurons increases, the time of calculation will also increase. At present, there is no clear method for the selection of the number of layers and neurons, and the deep network structure that meets the error requirements is obtained after many attempts based on specific problems. Table 2 shows the training set mean absolute error and test set mean absolute error of different neuron node numbers under the same hidden layer. Table 3 shows the influence of the number of hidden layers on the mean absolute error.

Table 2. The influence of the number of neuron nodes on the error

Serial number	Hidden layers	Number of hidden units	Epochs	Training set mean absolute error	Test set mean absolute error
1	2	7	200	4.99×10^{-5}	5.11×10^{-5}
2	2	8	200	4.18×10^{-5}	4.45×10^{-5}
3	2	9	200	4.02×10^{-5}	4.01×10^{-5}
4	2	10	200	3.85×10^{-5}	3.37×10^{-5}
5	2	11	200	3.45×10^{-5}	2.97×10^{-5}
6	2	12	200	3.55×10^{-5}	3.14×10^{-5}
7	2	13	200	3.46×10^{-5}	3.12×10^{-5}

Table 3. The influence of the number of hidden layers on the error

Serial number	Hidden layers	Number of hidden units	Epochs	Training set mean absolute error	Test set mean absolute error
1	3	11	200	3.44×10^{-5}	3.14×10^{-5}
2	4	11	200	1.08×10^{-5}	8.89×10^{-6}
3	5	11	200	5.87×10^{-6}	5.53×10^{-6}
4	6	11	200	7.81×10^{-6}	7.35×10^{-6}
5	7	11	200	7.01×10^{-6}	3.91×10^{-6}
6	8	11	200	6.89×10^{-6}	3.54×10^{-6}

Based on Tables 2 and 3, five hidden layers are selected, and the number of hidden units in each layer is 11. The activation function selects *ELU* function:

$$ELU(x) = \begin{cases} x, & x \geq 0; \\ e^x - 1, & x < 0; \end{cases} \quad (17)$$

the parameter optimiser selects Adam optimiser, the loss function selects *MSE* function:

$$MSE(\hat{y}, y) = \frac{\sum_{i=1}^n (y - \hat{y})^2}{n} \quad (18)$$

where n is the number of samples, \hat{y} is the label value, and y is the network estimate, the evaluation metrics select *MAE* function:

$$MAE(\hat{y}, y) = \frac{\sum_{i=1}^n |y_i - \hat{y}_i|}{n} \quad (19)$$

In addition to selecting the number of layers and nodes of the DNN, appropriate hyper-parameters (batch size and epochs) need to be selected during the training of the DNN. When the batch size is selected as 64, and epochs is selected as 500, the curve of average sum-of-squares error during the training set and the test set training histories is shown in Figs. 4 and 5.

To verify the accuracy of the trained DNN, 100 sample points are randomly selected and put into the trained network to obtain the remaining distance and remaining time. The study compared the remaining distance and remaining time obtained by the DNN with the remaining distance and remaining time obtained by integration, as shown in Figs. 6 and 7. Figures 8 and 9 are the absolute error curves of the remaining distance and remaining time fit by the DNN respectively. In Fig. 8, the maximum error of the remaining flight distance is 52 kilometers. In Fig. 9, the maximum error of the remaining flight time is 7.2 seconds. The error is within the allowed range for the HGV with a range of several thousand kilometers and a flying duration of several thousand seconds.

After the DNN is trained, the prediction can be replaced by the DNN, and the correction uses the binary Newton iteration method to solve the two parameters of the bank angle profile. In each guidance

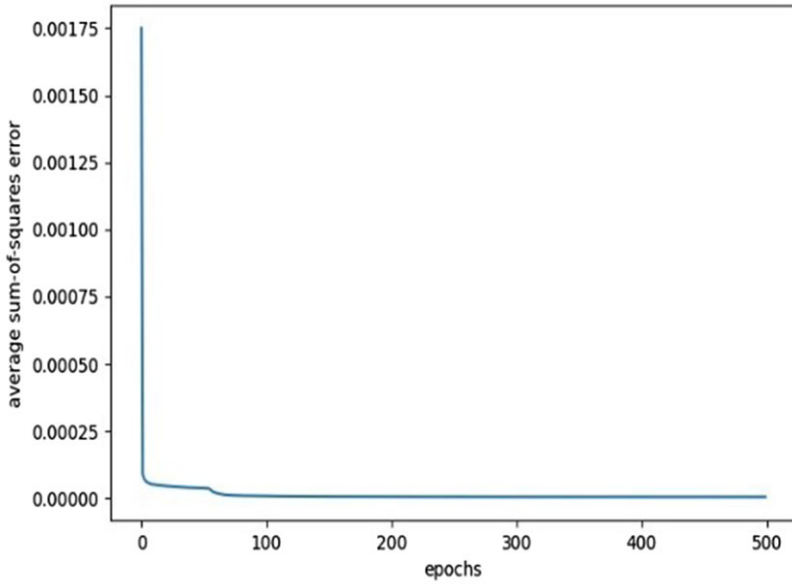


Figure 4. Training histories of the training set error.

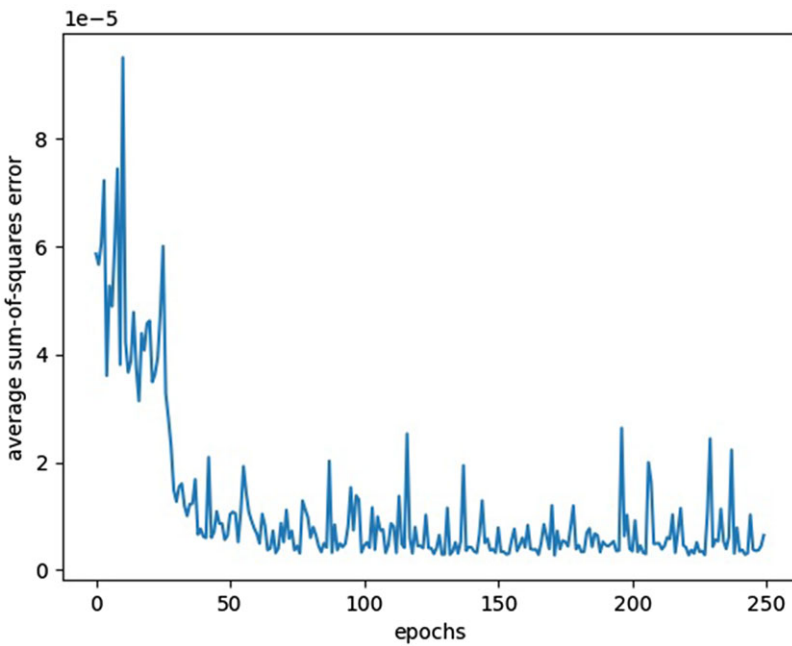


Figure 5. Training histories of the test set error.

cycle, the two parameters of the bank angle profile are corrected based on the constraints of distance and time.

$$\begin{cases} s_{NN} = s_f \\ t_{NN} = t_d \end{cases} \quad (20)$$

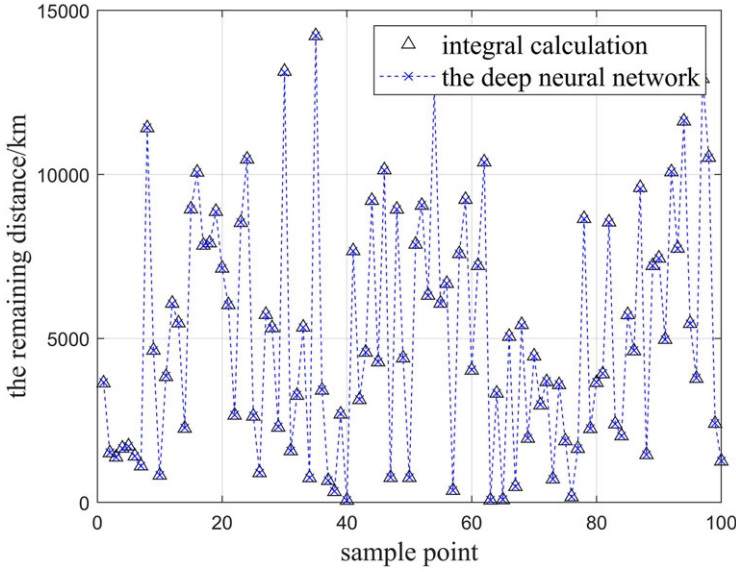


Figure 6. Fitting curve of the remaining distance.

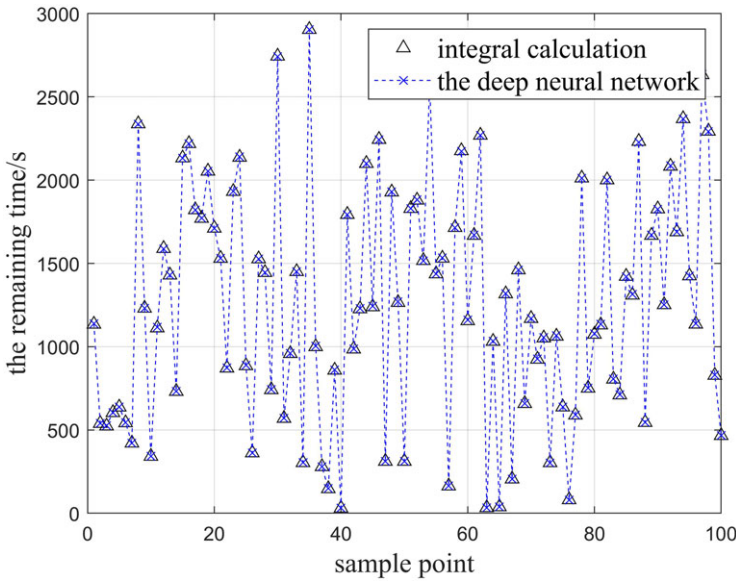


Figure 7. Fitting curve of the remaining time.

where s_{NN} is the remaining distance fitted by the DNN, s_f is the ideal remaining distance, it can be obtained from the current longitude and latitude and the terminal longitude and latitude; t_{NN} is the remaining time fitted by the DNN, t_d is the ideal remaining distance, it can be obtained by subtracting the elapsed time from the total time. Based on Equation (1), s_f and t_d can be obtained from the current state $x = [r \ \lambda \ \phi \ V \ \theta \ \psi \ t]$ of the vehicle:

$$s_f = \arccos(\sin \phi \sin \phi_f + \cos \phi \cos \phi_f \cos(\theta_f - \theta)) \tag{21}$$

$$t_d = t_{co} - t \tag{22}$$

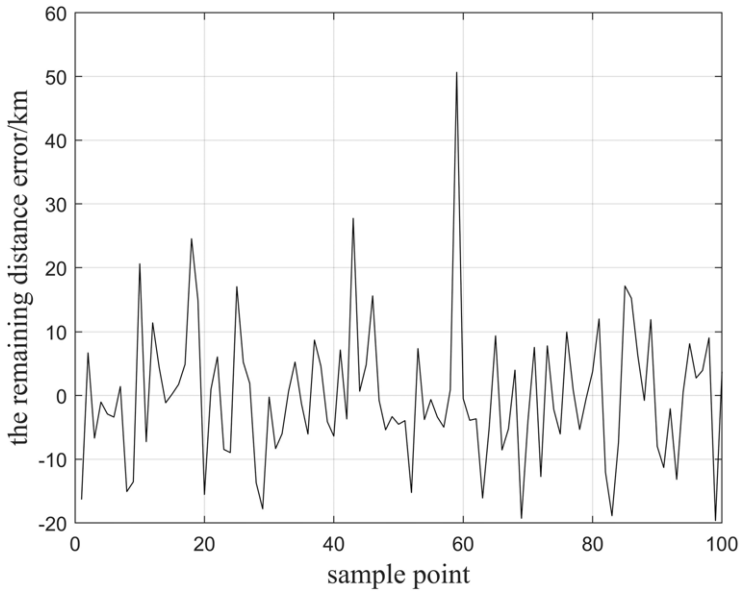


Figure 8. The remaining distance error of DNN.

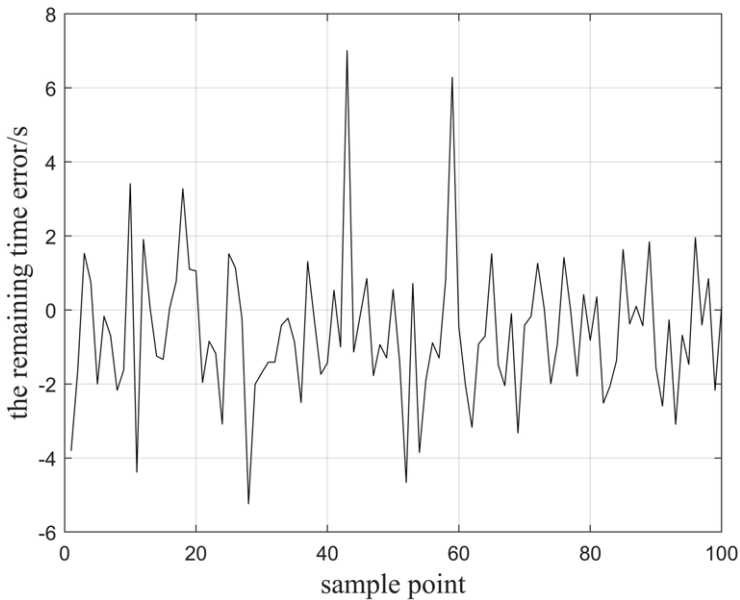


Figure 9. The remaining time error of DNN.

In Equations (21)–(22), s_f and t_d are known variables, s_{NN} and t_{NN} are adjusted by the input of the DNN, the input of the DNN can be changed by adjusting the two adjustment parameters of the bank angle profile. Therefore, Equation (20) can be transformed into a two-variable nonlinear system of equations:

$$\begin{cases} Q(\sigma_{mid}, \sigma_f) = s_{NN} - s_f = 0 \\ P(\sigma_{mid}, \sigma_f) = t_{NN} - t_d = 0 \end{cases} \tag{23}$$

Equation (23) can be solved by using the Newton iteration method of finding the roots of the binary nonlinear equation system.

$$\begin{cases} \sigma_{mid,k+1} = \sigma_{mid,k} + \frac{QP'_{\sigma_f} - PQ'_{\sigma_f}}{P'_{\sigma_{mid}}Q'_{\sigma_f} - Q'_{\sigma_{mid}}P'_{\sigma_f}} \\ \sigma_{f,k+1} = \sigma_{f,k} + \frac{PQ'_{\sigma_{mid}} - QP'_{\sigma_{mid}}}{P'_{\sigma_{mid}}Q'_{\sigma_f} - Q'_{\sigma_{mid}}P'_{\sigma_f}} \end{cases} \tag{24}$$

whereafter the initial values of σ_{mid} and σ_f are determined, σ_{mid} and σ_f of the next iteration are obtained from Equation (24). The initial values of σ_{mid} and σ_f of the next guidance cycle are the final values of σ_{mid} and σ_f of the previous guidance cycle. $Q'_{\sigma_{mid}}$, Q'_{σ_f} , $P'_{\sigma_{mid}}$ and P'_{σ_f} are the partial derivatives of Equation (23) concerning two parameters (σ_{mid} , σ_f), they can be obtained by finite difference approximation, for instance

$$Q'_{\sigma_{mid},k} = \frac{Q(\sigma_{mid,k} + \Delta, \sigma_{f,k}) - Q(\sigma_{mid,k}, \sigma_{f,k})}{\Delta} \tag{25}$$

where $\Delta > 0$ is a small constant. According to Equations (24)–(25), the values of iterative $\sigma_{mid,k}$ and $\sigma_{f,k}$ ($k = 1, 2, 3 \dots$) can be obtained. Substituting the values of $\sigma_{mid,k}$ and $\sigma_{f,k}$ into Equation (23), the DNN can quickly calculate the values of $Q(\sigma_{mid}, \sigma_f)$ and $P(\sigma_{mid}, \sigma_f)$. When the values of $Q(\sigma_{mid}, \sigma_f)$ and $P(\sigma_{mid}, \sigma_f)$ satisfy the following Equation (26), at this time, the final values of the two adjustment parameters of the bank angle profile in one guidance period can be obtained:

$$\begin{cases} Q(\sigma_{mid,k}, \sigma_{f,k}) < \varepsilon_1 \\ P(\sigma_{mid,k}, \sigma_{f,k}) < \varepsilon_2 \end{cases} \tag{26}$$

where ε_1 is the small error value of the distance, ε_2 is the small error value of the time.

3.4 Determining the sign of the bank angle based on the section heading angle corridor

This paper uses the heading angle corridor method to determine the sign of the bank angle for lateral guidance.

$$\psi_{Los} = \arctan \frac{\sin(\lambda_f - \lambda)}{\cos \phi \cos \phi_f - \sin \phi \cos(\lambda_f - \lambda)} \tag{27}$$

where ψ_{Los} is the line angle of sight from the current position of the vehicle to the target, λ and ϕ are the current latitude and longitude, they can be obtained from the current state $x = [r \ \lambda \ \phi \ V \ \theta \ \psi \ t]$. Therefore, the current heading angle error is that:

$$\Delta \psi = \psi - \psi_{los} \tag{28}$$

When the heading angle error exceeds the preset error corridor, the sign of the bank angle should be changed; otherwise, when the heading angle does not exceed the error corridor, the sign of the bank angle remains unchanged. In other words:

$$sign(\sigma_n) = \begin{cases} -1, \Delta \psi > \delta \psi \\ 1, \Delta \psi < -\delta \psi \\ sign(\sigma_{n-1}), -\delta \psi \leq \Delta \psi \leq \delta \psi \end{cases} \tag{29}$$

where σ_n is the current bank angle, σ_{n-1} is the bank angle of the previous moment, $\delta \psi$ is the preset heading angle error threshold. To control the accuracy of the landing point, this paper adopts a segmented

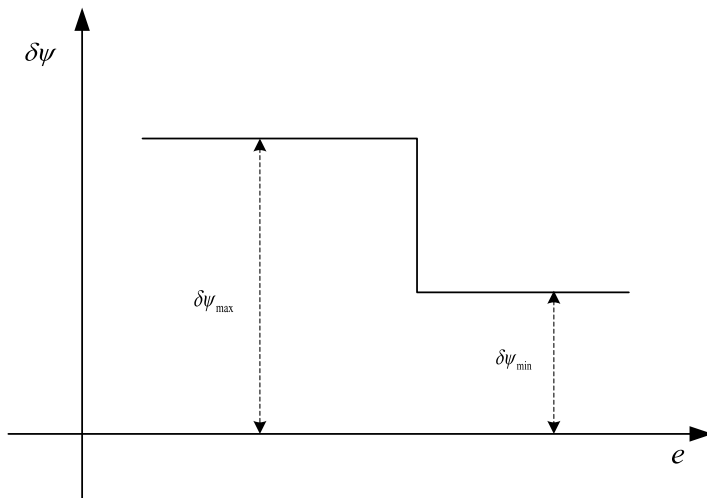


Figure 10. The segmented heading angle error threshold.

heading angle error threshold, the larger heading angle error threshold $\delta\psi_{\max}$ is adopted in the initial phase of flight, and the smaller heading angle error threshold $\delta\psi_{\min}$ is adopted in the phase of approaching the terminal energy, as Fig. 10 shows.

3.5 Aerodynamic parameter identification

The performance of the entry vehicle is reduced due to insufficient accuracy in the ground wind tunnel test or the pre-estimated aerodynamic characteristics of the aerodynamic calculation and the actual flight. In the design process of the DNN in this paper, the influence of the aerodynamic parameter disturbance (k_{cl} k_{cd}) has been taken into consideration and used as the input of the DNN. In order to obtain k_{cl} and k_{cd} in the guidance process, EKF is used for online aerodynamic identification.

The identification quantity is selected as the actual lift coefficient C_L and drag coefficient C_D , and it is considered that the change of lift coefficient and drag coefficient conforms to the Gauss-Markov process. The selected state quantity is $\vec{X} = [H \ V \ \theta \ C_L \ C_D]$, the state transition model can be obtained according to Equations (1)–(2), as shown in the Equation (30)

$$\vec{X} = f(\vec{X}) + \vec{\omega}_k = \begin{cases} \frac{d\hat{H}}{dt} = \hat{V} \sin \hat{\theta} + \omega_H \\ \frac{d\hat{V}}{dt} = -\frac{e^{-\frac{(r-R_e)}{h_s}} S \hat{V}^2 \rho_0 C_D}{2m} - g \sin \hat{\theta} + \omega_V \\ \frac{d\hat{\theta}}{dt} = -\frac{e^{-\frac{(r-R_e)}{h_s}} S \hat{V}^2 \rho_0 C_L \cos \sigma}{2m\hat{V}} - \frac{g \sin \hat{\theta}}{\hat{V}} + \frac{V \cos \hat{\theta}}{\hat{r}} + \omega_\theta \\ \frac{dC_L}{dt} = \omega_L \\ \frac{dC_D}{dt} = \omega_D \end{cases} \quad (30)$$

where $\vec{\omega} = [\omega_H \ \omega_V \ \omega_\theta \ \omega_L \ \omega_D]$ is the process noise of each state quantity.

The navigation system measures the relative velocity vector \vec{V} and the non-gravitational acceleration vector a_{Nav} , obtain the lift acceleration \vec{L} and drag acceleration \vec{D} , consider the real-time measurable

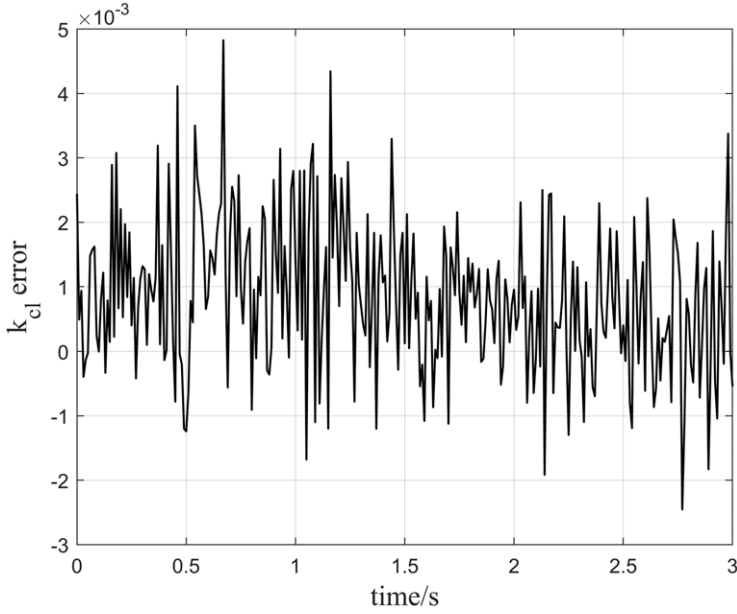


Figure 11. k_{cl} aerodynamic identification error.

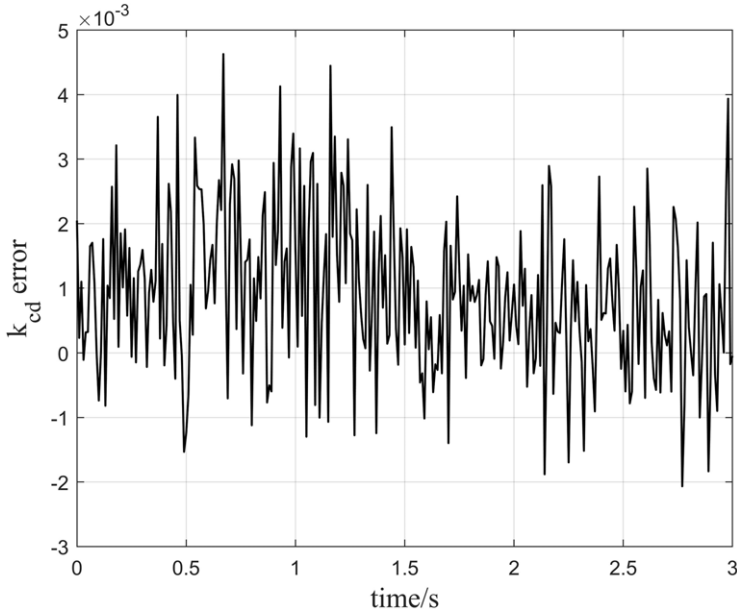


Figure 12. k_{cd} aerodynamic identification error.

height \tilde{H} , [30] and establish the observation model as

$$\vec{y} = f(\vec{X}) + \vec{v}_k = \begin{cases} \tilde{L}_c = \tilde{L} + v_L \\ \tilde{D}_c = \tilde{D} + v_D \\ \tilde{H}_c = \tilde{H} + v_H \\ \tilde{V}_c = \tilde{V} + v_V \end{cases} \quad (31)$$

Table 4. Time-coordination entry missions

Missions	Altitude (km)	Velocity (m/s)	Longitude (°)	Latitude (°)	Flight path angle (°)	Heading angle (°)	Time (s)
Vehicle 1	100.0	7,400.0	-144.3	40.0	-1.0	40.0	1850.0
Vehicle 2	100.0	7,400.0	-153.7	45.0	-1.0	40.0	1850.0
Vehicle 3	100.0	7,400.0	-148.7	45.0	-1.0	40.0	1850.0
Vehicle 4	100.0	7,400.0	-135.7	35.0	-1.0	40.0	1850.0
Terminal conditions	28.0	2,000.0	-32	37.0	-	-	-

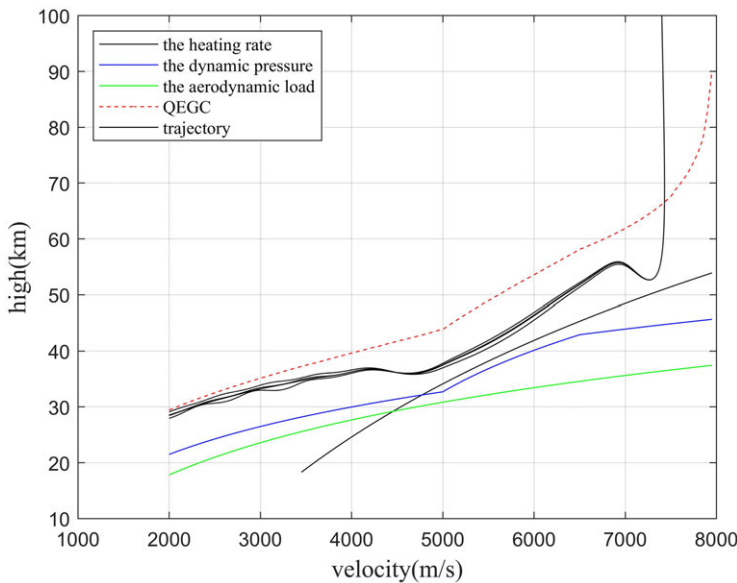


Figure 13. Altitude-velocity profile curve in nominal condition.

where $\tilde{L}_c, \tilde{D}_c, \tilde{H}_c, \tilde{V}_c$ are the measured values of lift acceleration, drag acceleration, altitude, and velocity respectively; $\tilde{v}_k = [v_L v_D v_H v_V]$ is the observation noise.

According to literature [31], an EKF is created and utilised to estimate the real lift coefficient and drag coefficient. The aerodynamic parameter disturbance coefficient is obtained by the ratio of the actual value of the lift coefficient C_L and the actual value of the drag coefficient C_D obtained by the identification of the nominal value of the lift coefficient C_{L0} and the nominal value of the drag coefficient C_{D0} obtained according to the literature [23]. In other words:

$$\begin{cases} k_{cl} = \frac{C_L}{C_{L0}} \\ k_{cd} = \frac{C_D}{C_{D0}} \end{cases} \quad (32)$$

The fluctuation range of the aerodynamic parameter correction coefficient is $[-20\%, 20\%]$, and the sine function $1+0.2\sin(\frac{2\pi}{3}t)$ used to characterise, error curve is obtained by comparing k_{cl} and k_{cd} obtained by aerodynamic identification with the true value is shown in Fig. 11 and Fig. 12. It can be seen from Figs. 11 and 12 that EKF can accurately estimate k_{cl} and k_{cd} .

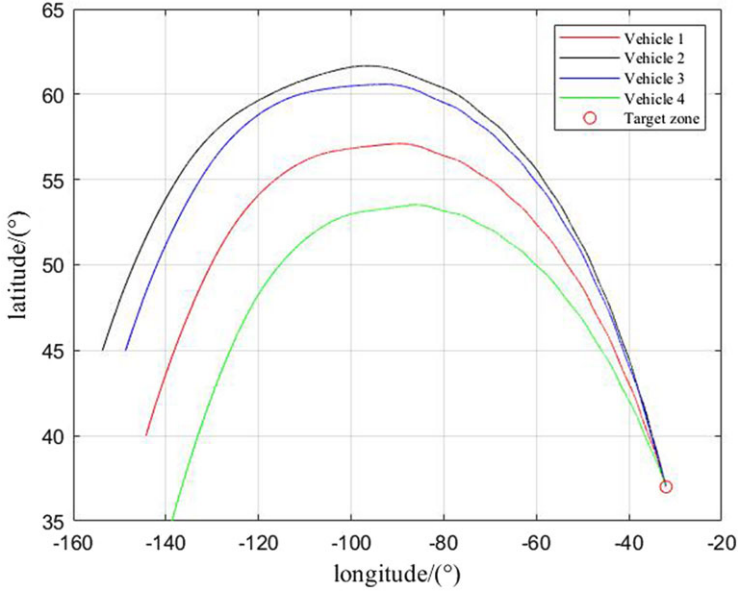


Figure 14. Ground track in nominal condition.

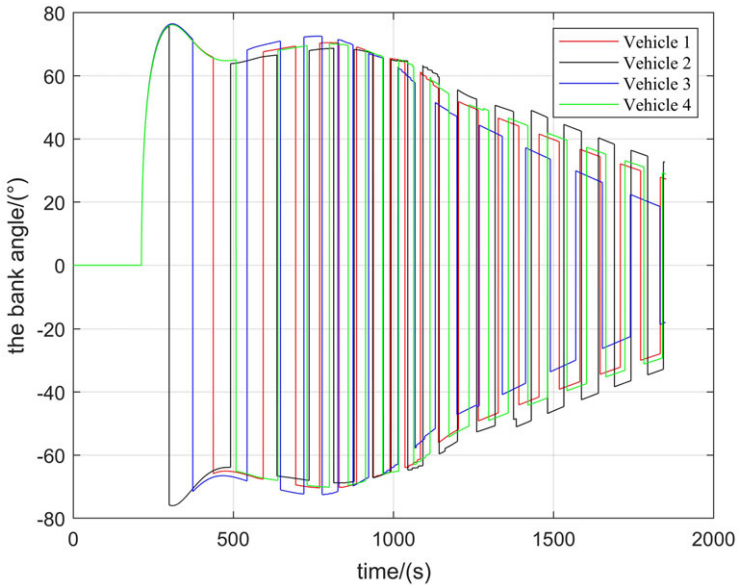


Figure 15. Bank angle profiles in nominal condition.

4.0 Simulation

The CAV-H vehicle selected for the entry vehicle model has a mass of 907kg and a reference area of $0.4838m^2$ [32]. The heating rate, aerodynamic overload, and dynamic pressure constraints are set as $\dot{Q}_{max} = 1000kw/m^2$, $n_{max} = 3g_0$, $q_{max} = 150kpa$ respectively. In the angle-of-attack profile, $\alpha_m = 20^\circ$, $\alpha_{L/D_{max}} = 10^\circ$. In the predictor-corrector, the iteration cut-off errors are $\epsilon_1 = 5km$ and $\epsilon_2 = 5s$. The initial values of the designed bank angle profiles are set as $\sigma_0 = 60^\circ$, $\sigma_{mid} = 70^\circ$, $\sigma_0 = 35^\circ$. The heading angle

Table 5. Terminal errors in nominal conditions

Vehicle	Velocity (m/s)	High (km)	Time (s)
1	-0.2237	0.5427	1.8000
2	-0.0416	-0.0987	-2.8000
3	1.0858	-0.0810	-0.2000
4	0.4422	-0.0276	0.7000

Table 6. Algorithm running time comparison

Vehicle	Time-coordination algorithm based on integral (ms)	Time-coordination algorithm based on the deep learning (ms)
1	37.7197	0.5064
2	36.6179	0.5006
3	44.0150	0.4995
4	36.8901	0.4990

Table 7. The perturbation settings in guidance simulation

Disturbance parameters	Δh_0	ΔV_0	$\Delta \lambda_0$	$\Delta \varphi_0$	$\Delta \theta_0$	$\Delta \psi_0$	ΔC_L	ΔC_D	Δm
Value	$\pm 5km$	$\pm 100m/s$	$\pm 2.0^\circ$	$\pm 2.0^\circ$	$\pm 0.2^\circ$	$\pm 1.0^\circ$	$\pm 10\%$	$\pm 10\%$	$\pm 3\%$

error threshold is set as $\delta\psi_{\max} = 10^\circ$, $\delta\psi_{\max} = 5^\circ$. In addition, the terminal cut-off condition is selected as the vehicle speed. In DNN, the batch size is set as 64, and the epochs are set as 500.

In the simulations, unless noted otherwise all the following numerical results are generated using a computer with AMD Ryzen 7 4800H processor (2.90 GHz, 8 cores, 16 threads), 16.0 GB memory, and a Windows operation system. The DNN training environment is PyCharm Community Edition, and the development language is Python, and the training framework is selected as tensorflow2.0.

4.1 Multi-task simulation under nominal conditions

Under nominal conditions, for the time-coordination entry mission based on deep learning of the hypersonic gliding vehicle, the four different initial positions of the vehicles in Table 4 are selected for simulation to verify the effectiveness of the algorithm.

The terminal status of each flight mission is shown in Table 4. Figures 13, 14 and 15 are numerical simulation images of each flight mission under nominal conditions. Figure 13 shows the high-velocity profile curve for different missions, the four curves all satisfy the Quasi-Equilibrium Guide Condition and path constraints. Figure 14 displays the ground track in nominal condition. Figure 15 is the bank angle profile in nominal condition, the terminal bank angle is gradually reduced to meet the time constraint. Table 5 shows the terminal errors based on deep learning. It can be seen that the terminal errors of each mission meet the error requirements. Table 6 compares the traditional integration algorithm with time-coordination algorithm based on deep learning in this paper for each guidance cycle. It should be noted that the algorithm proposed in this paper is only 2% of the loss time of the traditional integration algorithm.

Therefore, from the above simulation results, it can be seen that the time-coordination guidance algorithm based on deep learning proposed in this paper can meet the needs of multi-HGV entry coordination flight, and the addition of a DNN greatly improves the real-time performance of this algorithm.

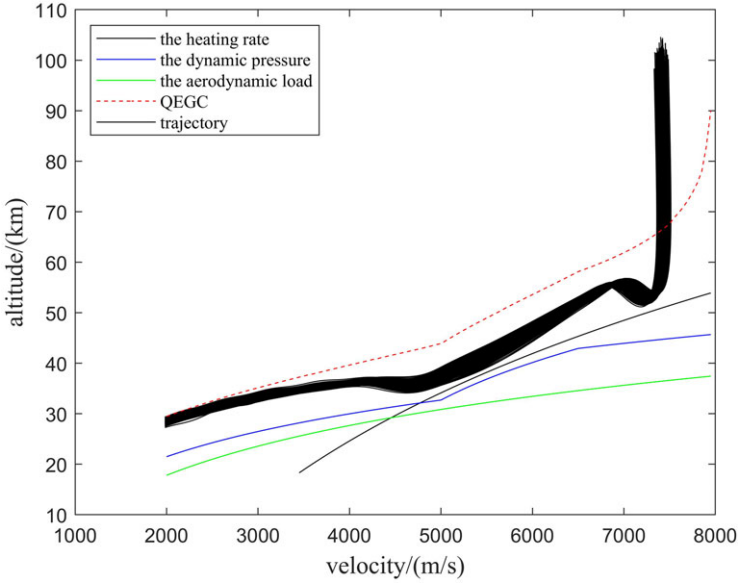


Figure 16. Altitude-velocity profiles curve for mission 4 under disturbance conditions.

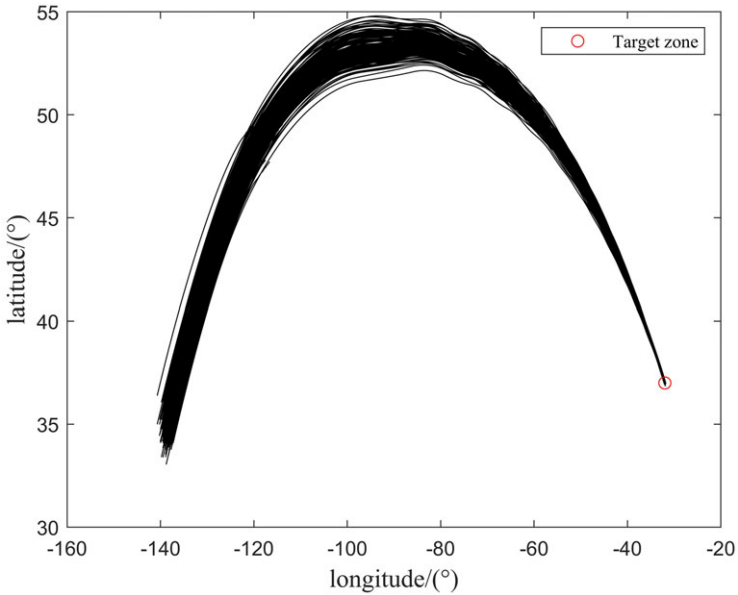


Figure 17. Ground tracks for mission 4 under disturbance conditions.

4.2 Multi-task simulation under disturbance conditions

The trained DNN itself has a certain amount of anti-interference ability; in this paper, the EKF is used to identify the aerodynamic parameters online and use them as the input for the DNN, which can greatly improve the robustness of the time-coordination guidance algorithm. To verify the robustness and accuracy of the time-coordination guidance algorithm based on deep learning, 200-run Monte Carlo

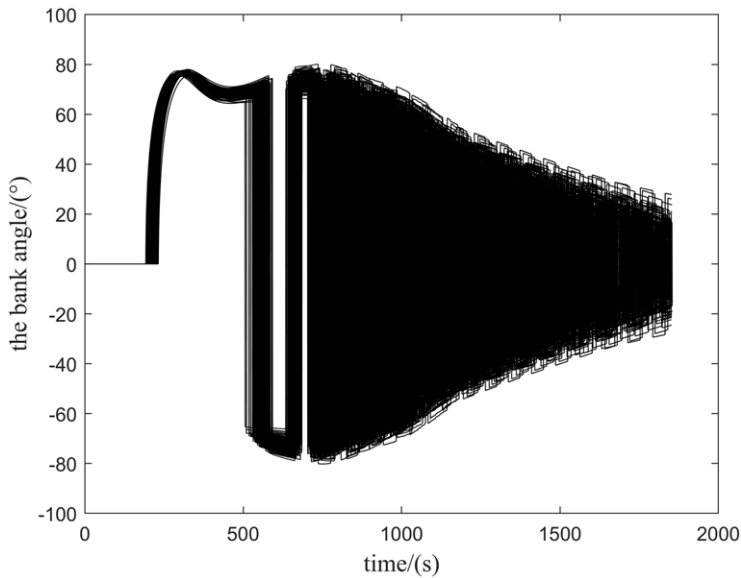


Figure 18. Bank angle profiles for mission 4 under disturbance conditions.

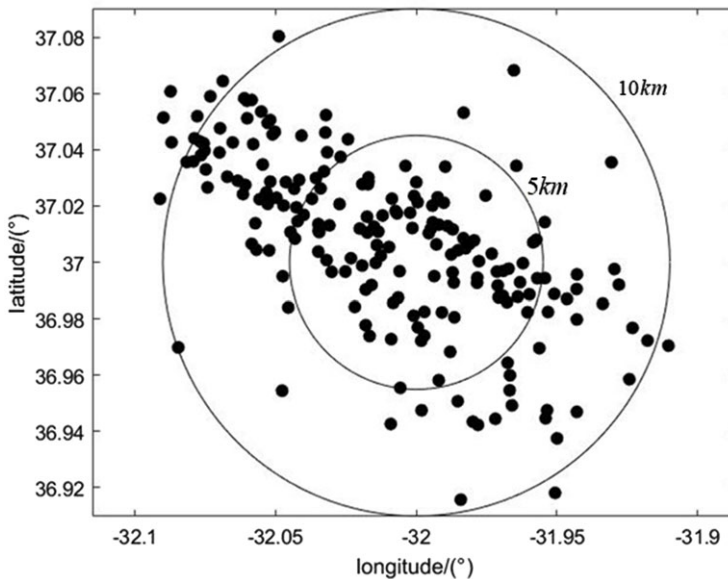


Figure 19. Falling point dispersion for mission 4 under disturbance conditions.

simulations are conducted on mission 4 in Table 4. The initial state deviations and parameter deviations in Table 7 conform to the normal distribution.

The numerical simulation results under disturbance conditions are shown in Figs. 16, 17, 18, 19, 20 and 21. Figure 16 displays the high-velocity profile curve for mission 4 under disturbance conditions, the curve shows that under disturbance conditions, the trajectory can still satisfy the path constraints and Quasi-Equilibrium Guide Condition. Figure 17 shows the ground tracks for mission 4 under disturbance conditions. Figure 18 displays the bank angle profiles for mission 4 under disturbance conditions,

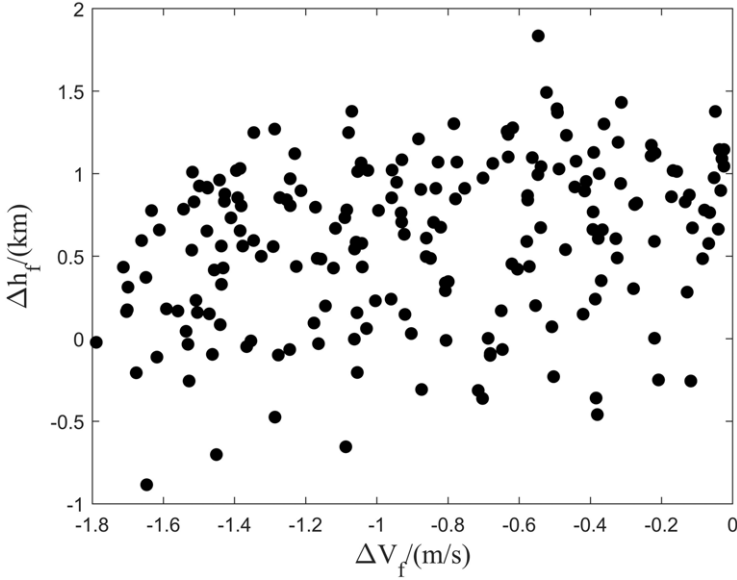


Figure 20. Terminal altitude-velocity error dispersion for mission 4 under disturbance conditions.

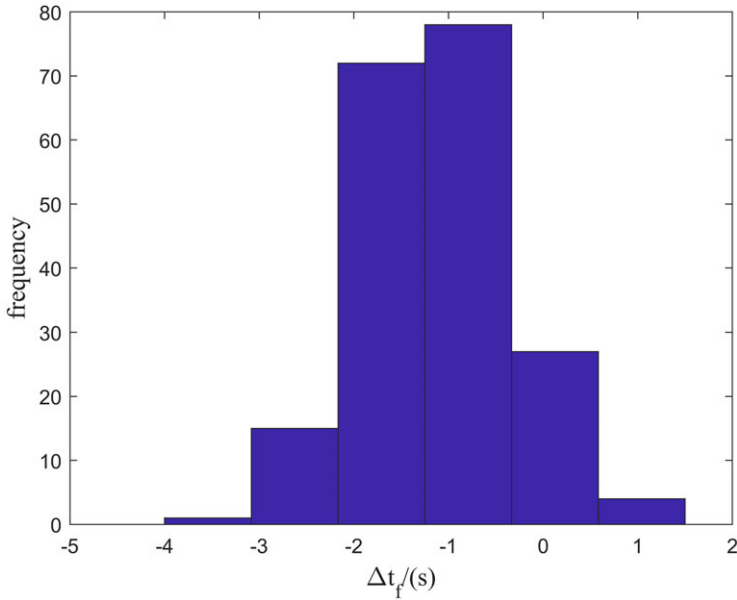


Figure 21. Histogram of terminal flight time errors for mission 4 under disturbance conditions.

it can be concluded that the bank angle can still fluctuate within a reasonable range under disturbance conditions. Figure 19 is the falling point dispersion for mission 4 under disturbance conditions, it can be seen that the terminal drop points are scattered along the flight direction, most of the landing points are within 5km, and the rest are within 10km, which meets the needs of entry guidance. Figure 20 shows the terminal altitude-velocity error dispersion for mission 4 under disturbance conditions. From Fig. 20, it is indicated that the terminal velocity error is within 1.8m/s, and the terminal altitude error is within 2km.

Figure 21 shows the histogram of terminal flight time errors for mission 4 under disturbance conditions, it indicates that the flight time error is within 4s.

Thus, it can be established from the simulation results that the time-coordination guidance algorithm based on deep learning proposed in this paper still has good guidance accuracy under the condition of initial state disturbance and parameter disturbance, proving the robustness of the algorithm in this paper.

5.0 Conclusion

This paper presented a guiding system for multi-hypersonic gliding vehicles that utilised DNN for guidance. A dual-parameter bank angle profile was used to suit the requirements of time coordination. To address the real-time needs of the HGV guiding algorithm, this research developed a range of DNN architectures and used error comparison to pick the network structure that was most suited for the situation at hand. A vehicle trajectory database was created and utilised to train the DNN structure that had been established. To enhance the algorithm's resilience, the EKF was employed to detect the disturbance coefficient of aerodynamic parameters online and utilised it as one of DNN the inputs to enhance the algorithm's anti-interference capacity. The simulation results using CAV-H vehicles demonstrated that the developed DNN structure was capable of meeting the temporal coordination requirements of several vehicles. Assuming the guiding accuracy matches the criteria, this method exhibited high resilience, excellent real-time performance, and the potential for online application.

Conflict of interest statement. The authors declare that there is no conflict of interest in this work.

References

- [1] Li, G., Zhang, H., & Tang, G. Flight-corridor analysis for hypersonic glide vehicles, *J Aerosp Eng*, January 2017, **30**, (1), p. 06016005.
- [2] Phillips, T.H. A common aero vehicle (CAV) model, description, and employment guide, *Schafer Corporation for AFRL and AFSPC*, 2003, 27.
- [3] Walker, S., Sherk, J., Shell, D., Schena, R., Bergman, J., & Gladbach, J. The DARPA/AF falcon program: The hypersonic technology vehicle#2 (HTV-2) flight demonstration phase, 15th AIAA International Space Planes and Hypersonic Systems and Technologies Conference, 2008.
- [4] Gao, Y., Zhang, M., & Jia, C. Development review of world air and missile defense system in 2016, *Tactical Missile Technol*, February 2017, (2), pp 16–20.
- [5] Liang, Z.X. *Research on three-dimensional guidance for maneuverable hypersonic gliding vehicles*, Beihang University, Beijing, 2016.
- [6] Shen, Z., & Lu, P. Onboard generation of three-dimensional constrained entry trajectories, *J Guid Cont Dynam*, May 2012, 2003, **26**, pp 111–121.
- [7] Zhang, Y.L., Chen, K.J., Liu, L.H., Tang, G.J., & Bao, W.M. Entry trajectory planning based on three-dimensional acceleration profile guidance, *Aerosp Sci Technol*, January 2016, 2016, **48**, pp 131–139.
- [8] Joshi, A., Sivan, K., & Amma, S.S. Predictor-corrector reentry guidance algorithm with path constraints for atmospheric entry vehicles, *J Guid Cont Dynam*, September 2007, **30**, (5), pp 1307–1318.
- [9] He, S., Wang, W., Lin, D. and Lei, H. Consensus-Based Two-Stage Salvo Attack Guidance, *IEEE Trans Aerosp Electron Syst*, June 2018, **54**, (3), pp 1555–1566.
- [10] Beard, R.W., McLaint, T.W., & Goodrich, M. Coordinated target assignment and intercept for unmanned air vehicles, *IEEE Trans Robot Automat*, December 2002, **18**, (6), pp 911–922.
- [11] Campbell, M.E., & Whitacre, W.W. Cooperative tracking using vision measurements on SeaScan UAVs, *IEEE Trans Contr Syst Technol*, July 2007, **15**, (4), pp 613–626.
- [12] Zong, Q., Wang, D., Shao, S., Zhang, B. and Yu, H. Research status and development of multi UAV coordinated formation flight control, *J Harbin Inst Technol*, March 2017, **49**, (3), pp 1–14.
- [13] Zhao, S.Y., Zhou, R. Multi-missile cooperative guidance using coordination variables. *Acta Aeronaut Astronaut Sin*, November 2008, **29**, (6), pp 1605–1611.
- [14] Zhang, Y.A., Ma, G.X., & Wang, X.P. Time-cooperative guidance for multi-missiles: A leader-follower strategy. *Acta Aeronaut Astronaut Sin*, June 2009, **30**, (6), pp 1109–1118.
- [15] Kumar, S.R., & Ghose, D. Cooperative rendezvous guidance using sliding mode control for interception of stationary targets, *IFAC Proc Vol*, 2014, **47**, (1), pp 477–483.
- [16] Liang, Z.X., Yu, J., Ren, Z., & Li, Q. Trajectory planning for cooperative flight of two hypersonic entry vehicles, 21st AIAA International Space Planes and Hypersonics Technologies Conference, American Institute of Aeronautics and Astronautics, Xiamen, China, 2017.

- [17] Yu, J.L., Dong, X.W., Li, Q.D., Ren, Z., & Lv, J.H. Cooperative guidance strategy for multiple hypersonic gliding vehicles system, *Chin J Aeronaut*, March 2020, **33**, (3), pp 990–1005.
- [18] Fang, K., Zhang, Q.Z., Kun, N.I., Cheng, L., & Huang, Y.T. Time-coordination reentry guidance law for hypersonic vehicle, *Acta Aeronaut Astronaut Sinica*, May 2018, **39**, (5), pp 202–217.
- [19] Zhang, W.Q., Yu, W.B., Li, J.L. and Chen, W.C. Cooperative reentry guidance for intelligent lateral maneuver of hypersonic vehicle based on downrange analytical solution, *Acta Armamentarii*, **July 2021**, **42**, (7), pp 1400–1411.
- [20] Wang, X., Guo, J., Tang, S.J., & Qi, S. Time-cooperative entry guidance based on analytical profile, *Acta Aeronaut Astronaut Sin*, March 2019, **40**, (3), pp 239–250.
- [21] Li, Z.H., He, B., Wang, M.H., Lin, H.S., & An, X.B. Time-coordination entry guidance for multi-hypersonic vehicles, *Aerosp Sci Technol*, June 2019, **89**, pp 123–135.
- [22] Mease, K.D., Chen, D.T., Teufel, P., & Schonenberger, H. Reduced-order entry trajectory planning for acceleration guidance, *J Guid Cont Dynam*, March 2002, **25**, (2), pp 257–266.
- [23] Jorris, T.R., & Cobb, R.G. Three-dimensional trajectory optimization satisfying waypoint and no-fly zone constraints, *J Guid Cont Dynam*, March 2009, **32**, (2), pp 551–572.
- [24] Lu, P. Entry guidance: A unified method, *J Guid Cont Dynam*, April 2014, **37**, (3), pp 713–728.
- [25] Li, Z.H., Hu, C., Ding, C.B., Liu, G., & He, B. Stochastic gradient particle swarm optimization based entry trajectory rapid planning for hypersonic glide vehicles, *Aerosp Sci Technol*, May 2018, **76**, pp 176–186.
- [26] Wang, X., Guo, J., Tang, S.J., Qi, S., & Wang, Z.Y. Entry trajectory planning with terminal full states constraints and multiple geographic constraints, *Aerosp Sci Technol*, January 2019, **84**, pp 620–631.
- [27] Rumelhart, D.E., Hinton, G.E., & Williams, R.J. Learning representations by back-propagating errors, *Nature*, October 1986, **323**, (6088), pp 533–536.
- [28] Li, J., & Zhang, M. On deep-learning-based geometric filtering in aerodynamic shape optimization, *Aerosp Sci Technol*, May 2021, **112**, p 106603.
- [29] Liu, Y., Wang, H., Fan, J., Wu, J., & Wu, T. Control-oriented UAV highly feasible trajectory planning: A deep learning method, *Aerosp Sci Technol*, March 2021, **110**, p 106435.
- [30] Shen, Z., & Lu, P. Dynamic lateral entry guidance logic, *J Guid Cont Dynam*, November 2004, **27**, (6), pp 949–959.
- [31] Evensen G. Sequential data assimilation with a nonlinear quasi-geostrophic model using Monte Carlo methods to forecast error statistics, *J Geophys Res*, May 1994, **99**, (C5), pp 10143–10162.
- [32] Phillips T.H. A common aero vehicle (CAV) model, description, and employment guide, Arlington, VA, US: Schafer Corporation for AFRL and AFSPC, 2003.